NANO · MICRO small
www.small-journal.com

Directional Cell Migration Guided by a Strain Gradient

Feiyu Yang, Pengcheng Chen, Han Jiang, Tianfa Xie, Yue Shao, Deok-Ho Kim, Bo Li,* and Yubing Sun*

Strain gradients widely exist in development and physiological activities. The directional movement of cells is essential for proper cell localization, and directional cell migration in responses to gradients of chemicals, rigidity, density, and topography of extracellular matrices have been well-established. However; it is unclear whether strain gradients imposed on cells are sufficient to drive directional cell migration. In this work, a programmable uniaxial cell stretch device is developed that creates controllable strain gradients without changing substrate stiffness or ligand distributions. It is demonstrated that over 60% of the single rat embryonic fibroblasts migrate toward the lower strain side in static and the 0.1 Hz cyclic stretch conditions at ≈4% per mm strain gradients. It is confirmed that such responses are distinct from durotaxis or haptotaxis. Focal adhesion analysis confirms higher rates of contact area and protrusion formation on the lower strain side of the cell. A 2D extended motor-clutch model is developed to demonstrate that the strain-introduced traction force determines integrin fibronectin pairs' catch-release dynamics, which drives such directional migration. Together, these results establish strain gradient as a novel cue to regulate directional cell migration and may provide new insights in development and tissue repairs.

1. Introduction

Cells are constantly exposed to mechanical strains due to tissue growth,[1] fluid flow,[2] muscle contraction,[3] etc. Numerous in vitro and in vivo studies support that mechanical strain is critically involved in various developmental and physiological processes, including the maturation of cardiac tissues, lung remodeling, and epithelial regeneration.[4,5] While the majority of current research focuses on the cellular responses to uniform strains, strain gradients also widely exist due to heterogeneous tissue mechanical properties and bending/torsional moment.[6,7] It has been observed in Xenopus ectoderm tissues that neuroepithelial cells collectively migrate along a strain gradient when subjected to concentrated loading, a process termed as "tensotaxis."[8] This phenomenon is drastically different from the extensively reported observation that cells reorientated under cyclic stretching.[9–11] However, it is still unclear whether tensotaxis also regulates the directional migration of mesenchymal-like cells.[12,13]

Directional cell migration can be guided by both biochemical and biomechanical cues in the cell microenvironment, including gradients of diffusible biomolecules (chemotaxis),[14] substrate bonded proteins (haptotaxis),[15,16] substrate topography (topotaxis),[17] and the stiffness of extracellular matrix (durotaxis).[18,19] Tensotaxis has yet been established as a biomechanical cue to guide directional cell migration, partially due to the difficulty of generating a controllable and physiologically relevant strain gradient (1–100% mm^{-1}),[20] and more importantly, the challenge to distinguish durotaxis and tensotaxis, as substrate stiffness changes with strain due to nonlinear material responses for many biomaterials.[21,22] Thus, tensotaxis and durotaxis are often used interchangeably, referring to the mechano-responsiveness of cells.[23]

Non-uniform strain fields have been generated using various approaches.[24–28] In those works, it is consistently reported that cell reorientation is a function of strain magnitude and cells tend to avoid strain gradient and angle perpendicular to the principal strain directions. However, none of the existing systems produce a consistent strain gradient. As a result, the tensotaxis behaviors have not been observed. In this work, we developed a novel strain gradient generation device by introducing void regions with defined geometries to a membrane. We used elastic polydimethylsiloxane (PDMS) membrane as the cell culture substrate to establish a strain gradient between 12% to 18%, which is within the linear regime of the stress-strain curve of the PDMS,[29,30] minimizing the possibility of generating a stiffness gradient caused by strain-stiffening or strain-softening effects. Arduino

F. Yang, H. Jiang, T. Xie, Y. Sun
Department of Mechanical and Industrial Engineering
University of Massachusetts Amherst
Amherst, MA 01003, USA
E-mail: ybsun@umass.edu
F. Yang, D.-H. Kim
Department of Biomedical Engineering
Johns Hopkins University
Baltimore, MD 21218, USA
P. Chen, Y. Shao, B. Li
Department of Engineering Mechanics
Tsinghua University
Beijing 100084, China
E-mail: libome@tsinghua.edu.cn
Y. Sun
Department of Biomedical Engineering
University of Massachusetts Amherst
Amherst, MA 01003, USA

The ORCID identification number(s) for the author(s) of this article can be found under https://doi.org/10.1002/smll.202302404

DOI: 10.1002/smll.202302404

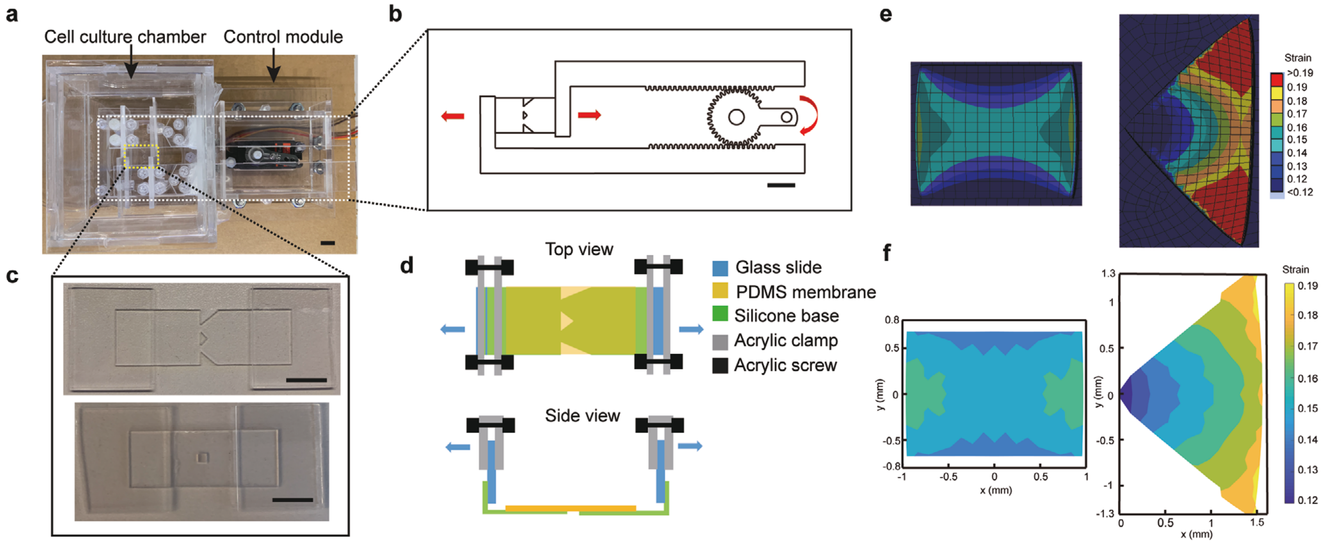

Figure 1. Design and calibration of the strain gradient generation device. a) Photo of the strain gradient generation device. Scale bar, 10 mm. b) Schematic showing the gear control mechanism. Scale bar, 10 mm. c) Photo of double-layer membranes with triangle cut-out (top) and square cut-out (bottom). Scale bar, 10 mm. d) Schematic showing device assembly and stretching application. e) Simulated strain fields for uniform strain (left) and strain gradient (right). f) Strain map showing experimental calibration of strain fields for uniform strain (left) and strain gradient (right).

microcontroller was used to precisely control the frequency and magnitude of uniaxial stretch with a servomotor. Using this device, we examined whether fibroblasts, which underwent constant stretches in vivo,[31] respond to strain gradients directly. We further analyzed the role of adhesions and the formation of protrusions in tensotaxis experimentally and computationally by developing an extended 2D motor clutch model.

2. Results

2.1. Design and Fabrication of the Device for Generating Strain Gradient

To study the effects of strain gradient on cell migration, it is essential to generate a controllable strain gradient to allow the migration of single cells in an optimal culture environment. Devices using microfluidic or vacuum to stretch cells can generate non-uniform strains. However, it is difficult to maintain a consistent strain field with a uniform gradient.[32,33] On the other hand, some systems require the encapsulation of cells in a sealed configuration.[34] It is difficult to maintain the oxygen, pH, and nutrition conditions at optimal levels for long-term cell culture, and the profusion flow may introduce undesired shear stress, causing unexpected cellular responses.[35]

To address these issues, we designed a new device for generating controllable strain gradients. This device was comprised of two primary components, the cell culture chamber and the control module (Figure 1a). In the control module, a programmable servo motor attached to a rotational gear was fixed in the middle. Two translational gears were tightly jointed with the rotational gear (Figure 1b). By controlling the rotational gear's motion on the servo motor, the translational gears were driven to perform a linear movement for uniaxial cell stretching. The strain gradients were generated by a double-layer membrane mounted at the end of the translational gears (Figure 1c). The bottom layer is a silicone film (1/32 in.) with cut-outs of desirable geometries produced by laser cutting. On the top of the silicone base, we plasma-bonded a layer of thin PDMS membrane. Two glass slides were plasma-bonded at both ends of the silicone base (Figure 1c). The advantage of this two-layer design is that the strain gradient can be modulated by the geometry of the cut-out, which is independent of the stretching magnitude and surface material properties. The assembly was mounted to the stretching device by clamping the two glass slides tightly with acrylic screws (Figure 1d). During the experiments, cells were seeded on the PDMS membrane in the area with the triangular and squire cut-off. A 60 mm petri dish was placed underneath to submerge the cell into culture media (Figure S1, Supporting Information).

2.2. Characterization of the Strain Field

To establish the correlation between the cut-out geometry and the strain gradient, we first used finite element analysis (Ansys) to simulate the strain field under uniaxial stretching. A graded and a uniform strain field were established on the cell culture areas for the triangular and square designs, respectively (Figure 1e). To validate the simulation results, we further sought to characterize the device by mapping the strain field experimentally. We applied the microcontact printing technique to print small markers with equal distance across the cell culture surface to calculate the strain across the cell culture area (Figure S2, Supporting Information). Images were taken before and after applying the stretch, and the displacement of markers was tracked using ImageJ (Figure S2a, Supporting Information). The strain and compression between two adjacent markers were calculated by dividing the change of distance by the initial distance in the x and y direction, respectively (Figure S2b, Supporting Information).

Consistent with the simulation results, we found that stretching the membrane with triangular cut-out by applying 15-degree rotation with the rotational gear led to strains between 12% to 18% across a horizontal distance of 1.5 mm, equivalent to a strain gradient of ≈4% mm^{-1}, while a uniform 15% strain was found for the membrane with square cut-out by applying 20-degree rotation with the rotational gear (Figure 1f; Figure S3, Supporting Information). Notably, the compression generated due to stretching was negligible (Figure S4, Supporting Information). As shown in Figures S3 and S4, Supporting Information, the sample-to-sample variations were small, suggesting this approach could reproducibly generate controllable strain gradients. The detailed experiment procedures and simulations can be found in the Experimental Section.

It is possible that after extended cell culture or cyclic stretching, the changes of the material properties of the membrane may influence the strain field. To evaluate the stability of the strain gradient under these experimental conditions, samples were calibrated first, submerged into 1× DPBS in a 37 °C incubator for 24 h, cyclic stretched at 0.1 Hz for 3 h, and then were calibrated again. We found no significant changes in the strain field, suggesting that in our experimental conditions, the strain field remained stable.

2.3. Establishing Strain Gradients with Uniform Stiffness and ECM Distributions

A strain gradient may lead to stiffness gradient if the materials show nonlinear strain-stiffening or strain-softening behaviors. To confirm that no such stiffness gradient was established on the double-layer membrane in the range of strain we plan to test (up to 18%), we obtained the stress-strain curve of the PDMS membrane using a soft material-specified tensile machine. Consistent with previous studies,[29,30] the range of the strain gradient for the double-layer membrane (12–18%) was within the linear regime of the PDMS stress–strain curve (Figure S5, Supporting Information). Therefore, the Young's modulus of the PDMS membrane remained constant at 0.827 MPa while the strain gradient was established in our system, excluding potential involvement of durotaxis.

A strain gradient on the membrane may also result in a nonuniform extracellular matrix (ECM) distribution if the membrane was coated prior to stretching. To minimize the effect of haptotaxis, for experimental groups with strain gradients imposed, we stretched the double-layer membrane to desirable strains and coated it with high concentration fibronectin (FN) (50 µg mL^{-1}) while it was stretched. The membrane was then released to relaxed status for cell seeding. After cell attachment, the membrane was re-stretched to apply strain gradient to the cells. To validate that the ECM molecules were distributed evenly under a strain gradient, we used HiLyte 488-labeled FN to directly visualize the FN distributions after stretching.[36,37] Our quantitative results showed that FN distributions remained uniform across the cell culturing area after applying a strain gradient to the cell (Figure S6, Supporting Information). Hence, our protocol successfully avoided introducing any ECM gradient, which minimized haptotactic cell migration.

2.4. REFs Migrate Directionally toward Lower Strain Direction

We next investigated whether the migration of single REFs could be influenced by the strain gradient. REFs were seeded on unstretched PDMS membranes with triangular and square cut-outs for 15 h to fully attach before applying a static stretching as shown in Figure 1f. The gradient and uniform conditions have a comparable average strain of 15%. The membranes were held at the stretched status for the next 6 h and cell migration trajectories were tracked using live-cell microscopy (Figure 2a; Videos S1–S5, Supporting Information). To avoid potential artifacts caused by membrane boundaries, only the cells in the center of the cell culture chamber were tracked. To minimize the influence of intercellular interactions, cells were seeded at a low density, and only samples with a total cell number of less than 170 cells were analyzed. Notably, only a few cells divided within the first 24 h after cell seeding, and the cells that divided during the experiment period would not be tracked.

To quantify the directionality of the cell migration relative to the strain gradient direction, we set up local coordinates for each cell with the x-axis being the maximum gradient direction (Figure 2b). We then connected the first and the last cell coordinates during the cell tracking period to calculate the migration angles. The cells were considered migrating toward the lower strain direction when the migration angle was between 90° to 270°. On the other hand, when the migration angle was between 0° to 90° or 270° to 360°, the cells were considered migrating toward the higher strain direction (Figure 2b). For the uniform strain conditions, as no strain gradient was established, the x-axis was set to be along the stretch direction.

Histograms were plotted for visualizing cell migration direction preferences (Figure 2c). We found 62.45% of cells migrating toward the lower strain direction in the static gradient group, which was significantly larger than the higher strain direction as confirmed by the Rayleigh test (Figure 2c). On the other hand, in the uniform strain condition, consistent with previous studies,[38,39] cells would prefer to migrate in the lateral direction during static stretch (Figure 2c; Figure S7a,b, Supporting Information). However, no unimodal preferences in the directionality of cell migration were found due to the lack of strain gradient (Figure 2c).

2.5. Tensotaxis Distinct from Topotaxis

When the PDMS membranes were stretched, the strain gradient could potentially lead to a variation of topography signals across the PDMS membrane, such as micro-size fibrillar structures which might affect cell migration preferences.[29,40] Indeed, after stretching the membrane a few times at the same magnitude, microscale wrinkles could be observed by confocal microscopy as shown in Figure S10, Supporting Information. Those wrinkles aligned perpendicularly to the stretch direction (Figure S10a, Supporting Information). We calculated the distance between adjacent wrinkles by analyzing the intensity profile (Figure S10b, Supporting Information) and calculated the frequency (number of wrinkles every 200 µm)

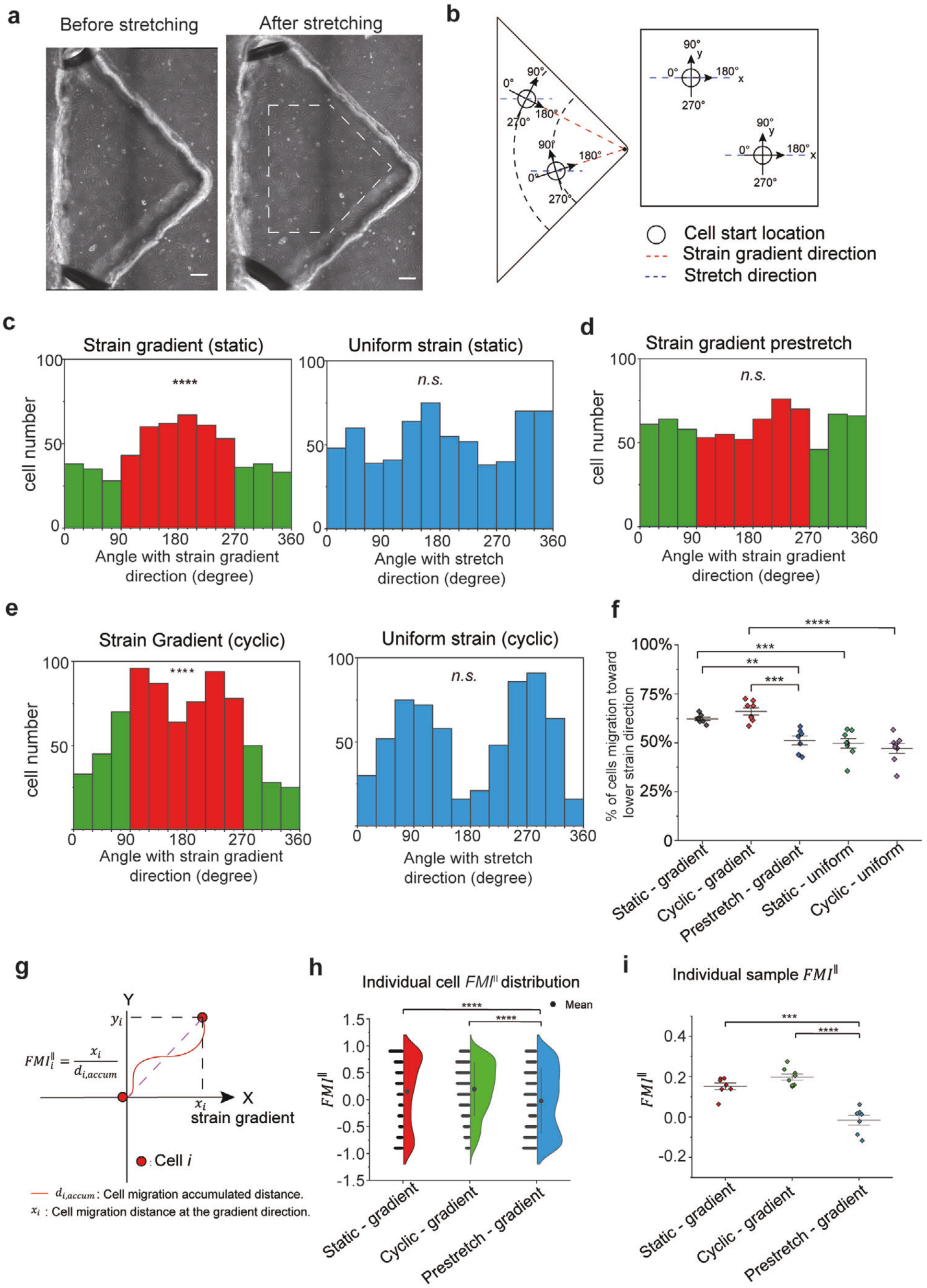

Figure 2. Tensotaxis behavior of REFs. a) Photos of REFs seeding on the gradient double layer membrane, before (left) and after (right) stretching. Region of interests was encircled with white dash lines. Scale bar, 200 µm. b) Schematics for the adjusted reference based on the cell's location on the gradient (left) and the uniform double-layer membrane (right). c–e) Histograms showing cell migration direction distributions under static strain gradient group (c, left, $N = 7$, $M = 554$), static uniform strain group (c, right, $N = 8$, $M = 654$), pre-stretched static strain gradient control group (d, $N = 7$, $M = 732$), cyclic strain gradient group (e, left, $N = 7$, $M = 649$), and cyclic uniform strain group (e, right, $N = 8$, $M = 630$). f) Individual sample's percentage of cells migrate to lower strain direction. Two sample t-tests were run between each pair of groups. g) Schematic showing the $FMI^{||}$ calculation. h) Violin plots show individual cell's $FMI^{||}$ distribution for static gradient group ($N = 7$, $M = 554$) (Mean = 0.158), cyclic gradient group ($N = 7$, $M = 649$) (Mean = 0.228), and pre-stretched strain gradient control group ($N = 7$, $M = 732$) (Mean = −0.022). Mann–Whitney tests were run between each pair of groups. i) Individual samples' average $FMI^{||}$ distribution for static gradient group ($N = 7$), cyclic gradient group ($N = 7$), and pre-stretched strain gradient control group ($N = 7$). Two sample t-tests were run between each pair of groups. Rayleigh tests were run to determine the unimodal distribution of the circular data. $^{**}p < 0.01$. $^{***}p < 0.001$. $^{****}p < 0.0001$. N: Sample number; M: Cell number.

along the stretch direction (Figure S10c, Supporting Information) using customized MATLAB codes. We found no significant difference in the wrinkle distribution from the tip to the end of the membrane, suggesting a lack of global topological cues.

To further exclude the influence of local topological cues, we design a pre-stretched static group as a control (Figure 2d; Figure S9b, Supporting Information). We first stretched the membrane and then coated it with FN to create a uniform ECM coating. We next seeded cells and tracked the cell migrations after 15 h of incubation. In this way, cells would not be subjected to stretch, therefore not being exposed to the strain and the strain gradient, while the condition of the substrates was the same as the static strain gradient group shown in Figure 2c, including any topological cues. No significant preference of cell migration was found in this pre-stretched condition, suggesting that cells directly sense the strain gradient imposed on cell bodies, rather than substrate material properties.

2.6. Cyclic Stretching Induces Cell Migration Perpendicular to Stretching Direction

We next investigated whether cyclic stretching induced different migration patterns. Both membranes with triangular and square cut-outs were cyclically stretched for the first 3 h at 0.1 Hz, then was held at the stretched status for the next 3 h. Interestingly, more cells migrated to the direction perpendicular to the strain gradient/stretching directions (migration angle close to 90° and 270°), compared to the static condition (Figure 2e). This trend is more prominent for the uniform strain condition (Figure 2e; Figure S7c, Supporting Information). However, under cyclic stretching conditions, we still observed a significantly high percentage of cells (66.35%) migrated toward the lower strain direction for the strain gradient condition (Figure 2e; Figure S9c, Supporting Information). These data suggested that cell reorientation to avoid strain gradients and tensotaxis are two independent, competing mechanisms to regulate directional cell migration upon stretching. This observation is further confirmed by the statistical analysis showing that biased cell migration toward the lower strain direction only existed in the presence of a strain gradient (Figure 2f).

2.7. Quantifying Tensotaxis Using the Forward Migration Index

We next evaluated the efficacy of the tensotaxis by quantifying the forward migration index ($FMI^{\parallel}$),[41,42] the ratio of the cell migration distance in the maximum gradient direction and the accumulated distance (Figure 2g). When the $FMI^{\parallel}$ was equal to 1 or −1, the cell migrated along or against the maximum gradient direction with no deviations, respectively. As such, a higher value of $FMI^{\parallel}$ represents a higher efficacy of tensotaxis response. Consistent with the histograms, we found that both static and cyclic stretching of cell-seeded samples with strain gradient led to more cells with the $FMI^{\parallel}$ closer to 1, with an average $FMI^{\parallel}$ of 0.158 and 0.228, respectively (Figure 2h,i). In comparison, the pre-stretched condition led to an average $FMI^{\parallel}$ closer to 0 (Figure 2h,i). Notably, the $FMI^{\parallel}$ for durotaxis of multiple cell types are smaller than 0.2,[43] suggesting that strain gradient is a potent cue to drive directional cell migration.

2.8. Quantitative Analysis of Individual Cell Migration Features

Having established the directionality of cell migration under the strain gradient, we further quantified important cell migration characteristics, including persistence (directness), migration distance, speed, velocity, and migration angle distributions at each timepoint. As shown in Figure S8, Supporting Information, the persistence of the cell trajectories was generally high, likely due to the short experiment timing (6 h) and limited migration distance (less than four cell bodies distances) (Figure S8c, Supporting Information). We also found that cells in the cyclic stretching groups showed lower directness, higher speed and migration distance compared with the static stretching groups (Figure S8b,d, Supporting Information), which were expected as cells tended to reorient and migrate more rapidly during cyclic stretching.[9,46] Moreover, we found the static-gradient group showed a higher persistence but similar speeds compared to the prestretch-gradient group (Figure S8b,d, Supporting Information). This is consistent with previous studies which demonstrated that static stretch would induce lateral migration along the principle stretch direction.[38,39]

We further analyzed the migration angle distribution at each time point. The directed lateral migration tendency was more prominent for the static uniform strain group (Figure S7a,b, Supporting Information). On the other hand, cells subjected to cyclic stretch showed a significant preference to reorient and migrate perpendicular to the stretch direction (Figure S7c, Supporting Information), which conforms to previous studies.[9,46] It is notable that for the static or cyclic gradient groups, cells would prefer to migrate toward the lower strain side along with lateral or perpendicular migration tendencies, respectively (Figure 2c,e). Moreover, the tensotaxis tendencies were significant starting at the first timepoint for both static and cyclic gradient groups (Figure S9a,c, Supporting Information). In contrast, no unimodal preferences in the directionality of cell migration were observed for the uniform strain groups (Figure 2c,e).

2.9. Strain Magnitude Regulates Tensotaxis Response Rate

We next investigated how strain magnitude regulated the tensotaxis. We divided each sample's cell culture area into four regions ($R1$ to $R4$) based on the strain magnitude (13.5–15%, 15–16%, 16–17%, and 17–18%) with a consistent strain gradient of about 4% mm^{-1}. (Figure 3a). We compared the $FMI^{\parallel}$ for cells in each region under static gradient, cyclic gradient, and pre-stretch conditions. As shown in Figure 3b,c, we found that in both static and cyclic gradient groups, the $FMI^{\parallel}$ was significantly larger for the cells in $R4$. We also observed trends of average $FMI^{\parallel}$ increasing from $R1$ to $R4$ for the static and cyclic groups (Figure 3e), suggesting a higher strain magnitude triggers a stronger tensotaxis response. No significant differences were found in the pre-stretched group. Together, these results suggest that a higher strain magnitude can increase the tensotaxis response rate.

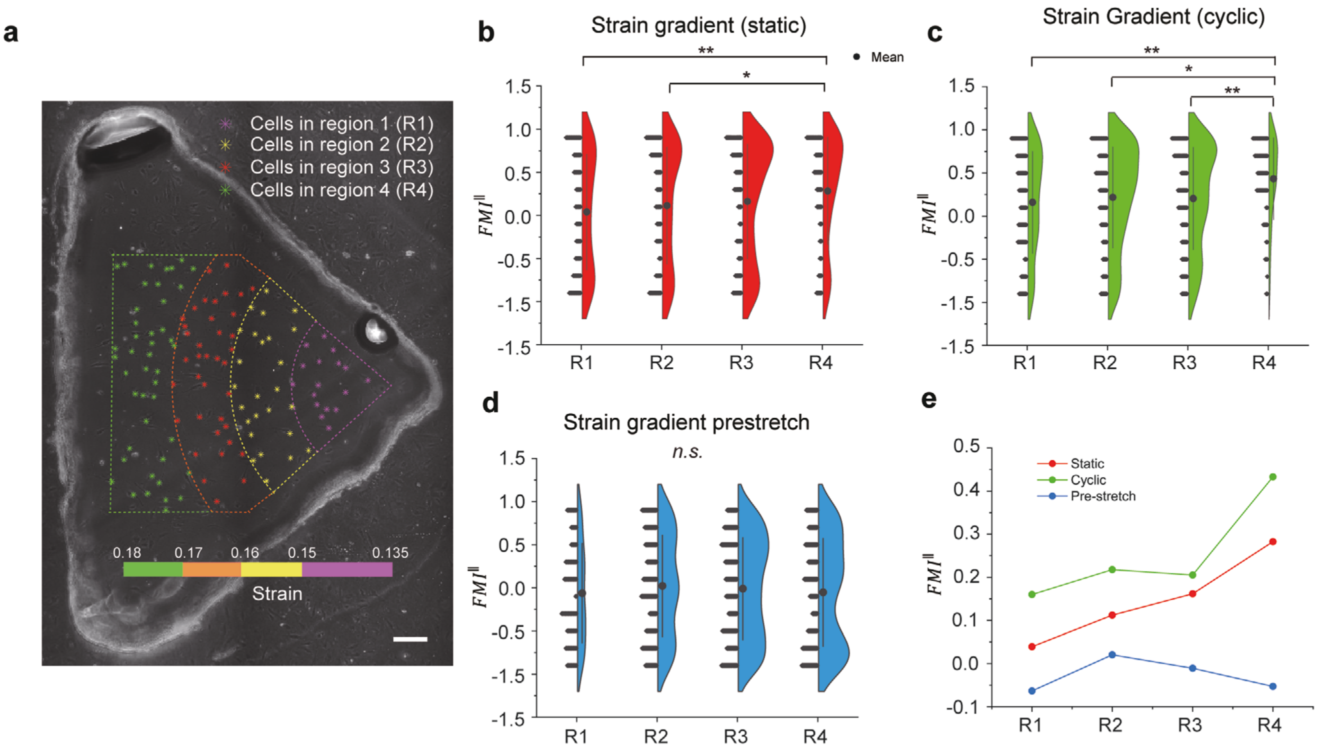

Figure 3. Strain magnitude regulates REF tensotaxis. a) Photo of dividing an individual gradient sample into four strain magnitude regions ($R1$–$R4$). Scale bar: 200 µm. b–d) Violin plots show individual cell's $FMI^{\parallel}$ distribution from $R1$ to $R4$ for the static gradient group (b, $N = 7$, $M1 = 94$, $M2 = 128$, $M3 = 201$, $M4 = 131$), cyclic gradient group (c, $N = 7$, $M1 = 116$, $M2 = 242$, $M3 = 223$, $M4 = 68$), and pre-stretched static gradient control group (d, $N = 7$, $M1 = 66$, $M2 = 171$, $M3 = 247$, $M4 = 248$). e) Individual cells' average $FMI^{\parallel}$ from $R1$ to $R4$ for the static gradient, cyclic gradient and pre-stretched control group. Mann–Whitney tests were run between each pair of groups. $*p < 0.05$, $**p < 0.01$. N: Sample number; $M1$: Cell quantity in $R1$; $M2$: Cell quantity in $R2$; $M3$: Cell quantity in $R3$; $M4$: Cell quantity in $R4$.

2.10. Increasing Focal Adhesion Formation and Cell Protrusion on the Lower Strain Side of Cells

We next investigated molecular mechanisms for the tensotaxis. As actin polymerization driven cell protrusion and the formation of new adhesion sites are the two most critical steps in cell locomotion,[44] we sought to investigate the directionality of single-cell protrusion and focal adhesion dynamics under a strain gradient. The REF52 cells we used were transfected with a YFP-Paxillin reporter,[45] and live-cell microscopy was used to evaluate the dynamics of paxillin containing focal adhesions. Cells cultured on membranes with triangular cut-outs were imaged before and 20 min after stretching (Figure 4a).

To analyze the focal adhesion dynamics as a function of strain gradient, we divided each cell into two halves along the axis passing the center of the cell nucleus and perpendicular to the strain gradient direction (blue line in Figure 4a). We used ImageJ to automatically identify each focal adhesion and quantified their sizes. After compensating for the imaging artifacts caused by stretching (see Experimental Section for details), we found that the total focal adhesion area increased significantly on the lower strain half compared with the higher strain half after stretching (Figure 4b).

We next quantified the cell protrusion and retraction on the lower and higher strain sides. We found that within 20 min after stretching, a significant protrusion on the lower strain half of the cell and retraction on the higher strain half could be found in the majority of cells analyzed (Figure 4c,d). By simultaneously analyzing focal adhesion dynamics and cell protrusion, we found that 62.5% of cells have both a higher rate of protrusion formation and a relative increase of focal adhesion contact area at the lower strain direction ($n = 16$), which conformed to the tensotaxis response rate shown in Figure 2c. Together, these results suggest that protrusion and preferential formation of focal adhesions on the lower strain side of the cell may lead to the tensotaxis of cells.

2.11. Actomyosin Contractility Is Required for the Tensotaxis Behavior

To confirm the involvement of actomyosin cytoskeleton in the tensotactic cell migration, Blebbistatin (Bleb), a highly specific inhibitor of non-muscle Myosin-II (NMII), was used to reduce cellular contractility and disassembly of focal adhesions through inhibition.[47] Previous studies have found that NMII inhibition would disrupt durotaxis.[48] and chemotaxis for some cell types.[49] Here, we treated the REFs with 50 µM of Bleb for 1 h before applying the static strain gradient. We visualized prominent contracting and shape-changing of the REF cells (Figure S11a,b, Supporting Information). Then we tracked cell migration directions for the following three hours. Quantitative results revealed no migration preferences for the Bleb-treated strain

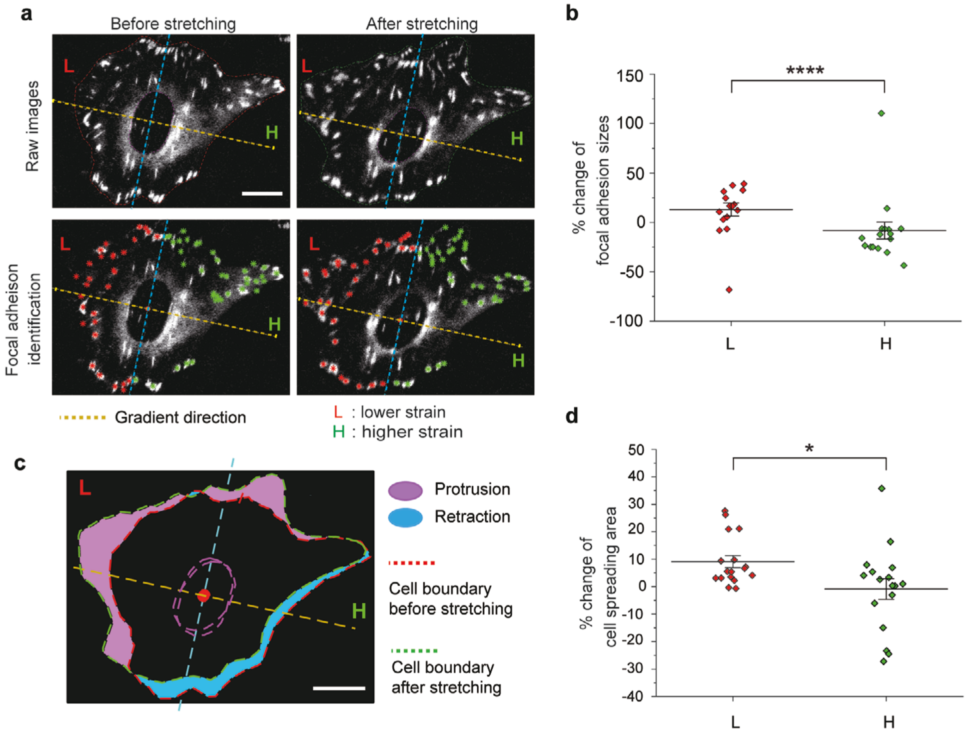

Figure 4. Focal adhesion dynamics and polarized cell protrusion in response to strain gradient. a) Raw images (top) and focal adhesions identified images (bottom) of a representative REF before (left) and after (right) stretching. Scale bar 20 µm. b) Normalized percentage change of the total focal adhesion area in the lower and higher strain halves of the cells ($N = 16$). c) Overlapping the images before and after stretching by the nucleus center (red dot) and the gradient direction (yellow dash line). The protrusions (purple) and retractions (blue) after stretching were color coded. d) Percentage of cell area change in the lower and higher strain half ($N = 17$). Two sample t-tests were run. $^*p < 0.05$. $^{****}p < 0.0001$. N: cell number.

gradient group (Figure S11c, Supporting Information). Moreover, consistent with previous studies,[50,51] we found higher cell motility compared with the static strain group (Figure S11d, Supporting Information).

2.12. Extended Motor-Clutch Model Recapitulates Tensotaxis

To explain the mechanism of the tensotaxis behavior governed by focal adhesion dynamics, we developed a modified version of the extended 2D motor-clutch model (EMM).[52,53] We propose that the cell motility is determined by the catch-release dynamics of integrin and FN pairs, which are partially governed by strain gradient dependent cell traction forces. Here, an individual REF is modeled as a polygon attached to a stretched elastic substrate (Figure 5a), whose vertexes are connected by springs. The actin filaments connect the cell vertexes to the nucleus centroid (Figure 5b). By incorporating the EMM with each filament to quantify the on-rate of integrin-FN bonds (k_{on}), we found that the higher affinity of bonds appears on the lower strain side of the substrate, which is consistent with the focal adhesion dynamics observed in the experiment. We then simulated the migration of an individual REF coupled with 34 vertexes on a 4% strain gradient substrate for 6 h. We confirmed that the EMM is sufficient to recapitulate the directional cell migrations (Figure 5c,d).

We further verified the consistency between EMM and experiment results by calculating the life time percentage $\alpha = \Delta t/T$, where Δt is the total time of engaging for integrin-FN pairs and T is the whole simulation time. As shown in Figure 5e, longer lifetime of integrin-FN bonds is observed on the lower strain regions, resulting in focal adhesions with longer life spans and larger sizes. This result suggests higher traction and slower retrogradation speed of actin filament on the side with lower strain (Figure 5f), which enables cell protrusion toward lower strain region. Together, our extended motor-clutch model can well recapitulate cell tensotaxis behaviors observed in our experiments.

3. Discussion

Cell migration in vivo is an essential process during development and normal physiological activities, which requires precise guidance to ensure proper cell localizations. Durotaxis, topotaxis, and haptotaxis are prominent examples of how mechanical properties and ligand distributions of ECM direct cell migration. However, the role of active mechanical forces and consequently, mechanical deformations of tissues has not been rigorously studied. Heterogeneous strain field, or strain gradient, can be established in bending deformation or in tissues with heterogeneous mechanical properties. Experimental systems that can effectively decouple matrix mechanics and ligand distributions from strain gradients are critical for rigorously studying this issue. In this work, we designed a novel strain gradient generation device that could generate a continuous strain gradient in mm scale for long-term cell migration tracking, distinct from the non-uniform strain field

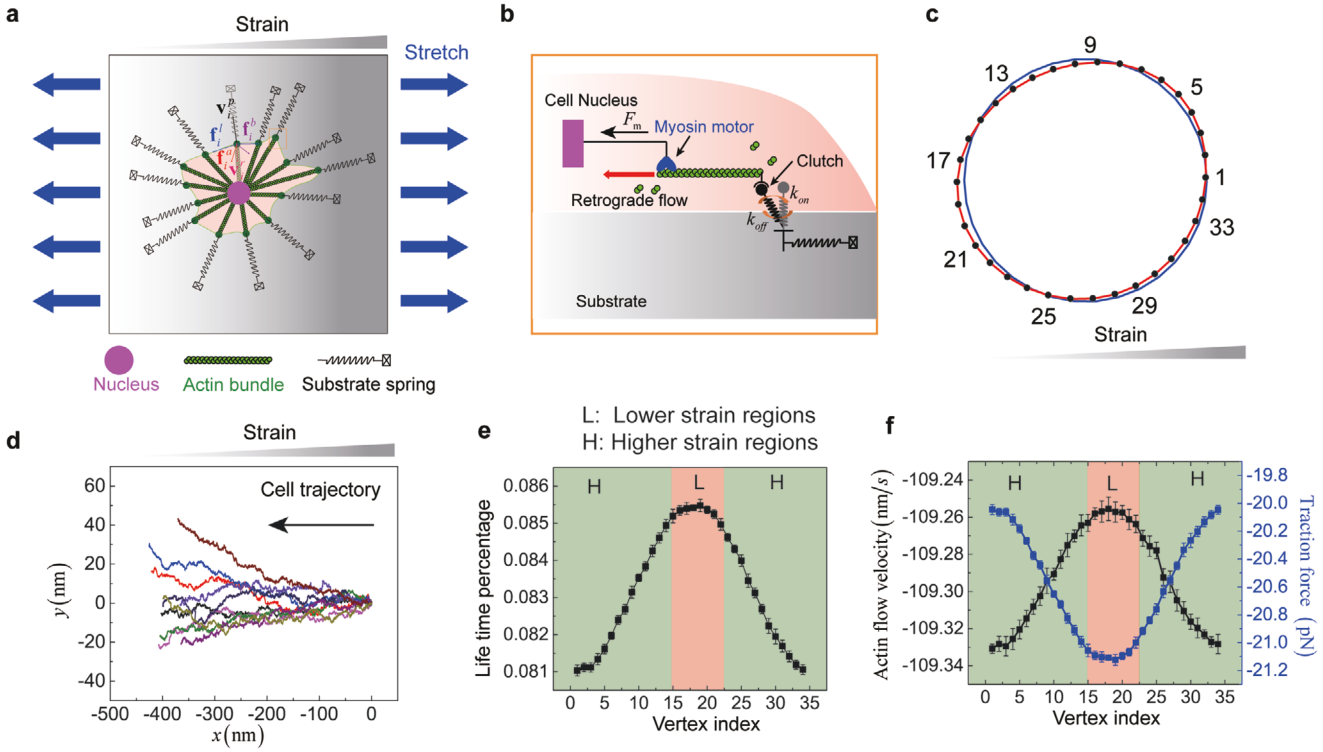

Figure 5. Extended 2D motor-clutch modeling simulates tensotaxis. a) Schematic of a cell model. b) Motor-clutch module of an individual vertex. c) Schematic of a simulated cell model migrating from (blue line) to (red line) on a 4% gradient of strain substrate. The cell centroid is located on the 15% strain region. Black dots are cell vertex. The numbers indicate the vertex index. d) Representative of predicted cell trajectories on the 4% gradient of strain substrate ($N = 10$). Cell centroid ($x = 0$, $y = 0$) is located on 15% strain region. e) Life time percentage of f) engaged integrin-fibronectin pairs and traction force, and actin retrogradation flow velocity during cell migration. Red and green regions represent the lower and high strain side, respectively. N: cell number.

generated by applying concentrated forces.[27] As the strain gradient can be tuned by changing the geometry of the cut-out in the underlying silicone layer without altering stretching parameters, the strain gradient and stretching magnitude, frequency, strain rate, and surface material properties can be controlled independently. No shear forces caused by the flow of media or air were introduced into the system. Compared to microfluidic-based and commercially available cell stretchers, our device is facile to fabricate without the need for cleanroom facilities and completely biocompatible, making it suitable for broader adaptations. Future works shall focus on modifying the device to study how strain gradient and other strain parameters synergistically regulate cell migration and other cell functions such as stem cell differentiation.

Our experiment clearly demonstrated that tensotaxis is distinct from durotaxis and haptotaxis. As the strain range we tested was within the linear regime of the stress-strain curve of PDMS,[29,30] no strain-stiffening/softening was generated to induce durotaxis (Figure S5, Supporting Information). Additionally, durotaxis was generally investigated using soft hydrogels (E = 2–7 kPa) due to the narrow range of stiffness cells can typically sense.[18] The PDMS membrane has a stiffness of 0.827 MPa, which is too stiff for cells to show significant durotaxis even minor strain-stiffening/softening exists. On the other hand, to decouple the effects of heterogeneous ECM ligand distributions, we coated ECM molecules while the membrane was stretched, and direct visualization of HiLyte 488 conjugated FN distributions clearly demonstrated the uniformity of ECM after stretching (Figure S6, Supporting Information). Moreover, in the control group (Figure 2d), we pre-stretched the membrane and seeded cells on stretched membranes, which show no preferences for cell migrations. Those well-controlled conditions excluded any potential influences of topotaxis or haptotaxis signals.

It has been established that cells utilize mechanosensitive focal adhesions,[53–55] filopodia structures,[56] and contractile machinery.[57] in their rigidity sensing. Our results in Figures 4 and 5 also showed that the focal adhesions were sensitive to strain and the stability and/or formation of new focal adhesions were preferred in regions with lower strain, which may facilitate the protrusion of cells toward lower strain direction. Moreover, we found that Bleb-treatment would disrupt tensotaxis due to the loss of contractility and disassembling of focal adhesions (Figure S11, Supporting Information). One possible explanation is the catch-slip bond-like behaviors observed in focal adhesions,[45] Smaller strain may lead to a force-dependent stabilization of focal adhesions (“catch”), while larger strain may lead to the dissociation of focal adhesions (slip). As such, we have confirmed the hypothesis through a modified version of the classic motor-clutch model, demonstrating that the strain gradient would control the binding and unbinding of integrin-FN bonds resulting in directional migration.

In conclusion, by generating a controllable strain gradient on cells, we demonstrated cells directly respond to a small strain gradient (≈4% mm^{-1}) and migrate directionally toward the lower strain. This mechanosensitive behavior, termed tensotaxis, is distinct from durotaxis or haptotaxis, and depends on the magnitude of the strain applied to the cells. Subcellular analysis revealed that lower strain increases the levels of focal adhesions and facilitates cell spreading. Simulations suggest that gradient-induced traction variation would determine the binding and unbinding of integrin-FN bonds, which drive the tensotaxis of cells. Together, we establish the strain gradient as a mechanical cue to guide the directional migration of single cells and provide insights into the mechanisms of tissue remodeling and morphogenesis. Our results demonstrate that the tensotaxis of cells depends on the magnitude of strain and is initiated by strain dependent focal adhesion formation and cell protrusion.

4. Experimental Section

Device and Double-Layer Membrane Fabrication: Parts of the cell stretching device were printed with a laser cutter (40 Watt Epilog Mini 18 × 12) using the acrylic sheet (Figure 1a), and assembled with screws and sealed with PDMS. In the control module, a programmable servomotor (DS3218, Annimos) attached with a rotational gear was fixed in the middle. The Arduino Uno microcontroller was adopted to control the servomotor. Two translational gears were properly joined with the rotational gear on two sides, which were designed to connect the cell culture chamber with the control panel (Figure 1b). Two small openings in between allowed the translational gears to extend into the cell culture chamber. Parafilms (PM-996, Bemis) were wrapped around the translational gears to seal the openings (Figure S1, Supporting Information).

The cell culture chamber was encapsulated to create a contamination-free, biocompatible environment. The chamber could be opened from the top and the bottom (Figure S1, Supporting Information). A removable lid was designed to cover the top of the chamber, and small gaps were left to access air. On the bottom, an opening was made below the double-layer membrane, which was sealed with a removable acrylic sheet by screws.

The double-layer membrane was fabricated with 1/32 in silicone film, PDMS membrane, plasma bonded on two glass slides at both ends (Figure 1c; Figure S12a, Supporting Information). The silicone film (base layer) was cut through with a laser cutter to create desired shapes. Dow Corning Sylgard 184 silicone elastomer and cure agent (GMID: 04019862) were mixed in the 10:1 ratio to fabricate the PDMS membrane (top layer). A small amount (<500 µL) of PDMS was pipetted on the center of an Ø85 mm acrylic circle. The PDMS was spin-coated the acrylic circle at 500 RPM for 30 s and then at 1000 RPM for another 2 min (WS650MZ23NPPB, Laurell Technologies). PDMS-coated acrylic circles were cured in a 65 °C oven overnight. A thin layer of PDMS membrane with a thickness of around 100 µm was formed on top of the acrylic circle. The thickness was measured with a precise micrometer (293-340330, Mitutoyo). The PDMS coated acrylic was laser cut into 22 × 14 mm and 14 × 14 mm pieces for the triangular and the squire cut-off, respectively (Figure 1c). The glass slide (125444, Fisher Scientific) was cut into 20 × 25 mm pieces. Acrylic template was laser printed in the shape of the double-layer membrane for precise alignment (Figure S12, Supporting Information). All parts were cleaned with 100% ethanol. The silicone film base, PDMS membrane, and glass slides were bonded with a plasma cleaner (PDC-001, Harrick plasma) at 500 psi for 3 min, then baked at 65 °C overnight for firm bonding. The dimensions of the designs were illustrated in Figure S13, Supporting Information.

REF Cell Culture in the Cell Stretching Device: REF-52 expressing YFP-paxillin fusion protein (a gift from Dr. Jianping Fu) were cultured in T-25 flasks and subcultured at 90% confluency. The culture media were composed of DMEM (11960051, Gibco) supplemented with 10% FBS (10082147, Gibco), 1% MEM NEAA (11140050, Gibco), 1% GlutaMAX (35050061, Gibco), and 1% Penicillin Streptomycin (15140122, Gibco).

To prepare the device for cell seeding. The double-layer membrane was first sonicated for 5 min in 100% ethanol to remove all particles on the surface, and then sterilized by autoclaving. The cell stretch device was sprayed with 70% ethanol, then blow-dried in a biosafety cabinet. The membrane was then mounted onto the device and cyclically stretched a few times for testing. To avoid the effect of haptotaxis, the membranes were stretched to the desired magnitudes before coating FN. The membranes were incubated at room temperature with 50 µg mL^{-1} FN (33016-015, Gibco) for 1 h by pipetting 100 µL solution on the cell culture area, which was then rinsed off with 1× DPBS.

REFs were seeded at the density of 50 K to 80 K mL^{-1} by pipetting 100 µL cell suspensions on top of the cell culture chamber. The device was then placed into a 37 °C incubator for 1 h for cell attachment, and then 5 mL culture media were added to submerge the cells for overnight incubation. For Bleb-treated static gradient group, REFs were treated with 50 µм Bleb for 1 h before applying the strain gradient. The stretching and imaging procedures would begin 15 h after cell seeding.

Finite Element Analysis: Finite element modeling of the double-layer membrane was conducted using the Ansys simulation software. Two-layer 3D models were constructed to mimic the structures of the double-layer membrane (Figure S14a, Supporting Information). The PDMS membrane was defined to bond on top of the silicone base (Figure S14b, Supporting Information). For simplicity, only the cell seeding chamber was modeled. For the silicone film, a tensile test was conducted to acquire the test stress-strain data (Mark-10 Force Gauge Model M7-5), which was curve-fitted using the polynomial 2nd order equation in the simulation (Figure S14c, Supporting Information). For the PDMS membrane, the material properties were defined based on previous literature,[58] with Young's modulus set to 1.1 MPa, the Poisson's ratio to 0.45, and density to 970 kg m^{-3}.

In the simulation, the forces applied in the *x*-direction were estimated to conform to the experimental strain magnitude across the cell culture area. To mimic the uniaxial stretching, forces were applied on both sides of the models (Figure S14a, Supporting Information). The parameters of the simulation were described in Table S2, Supporting Information.

Strain Field Calibration: To quantify the strain across the cell culture area, patterns of small markers (Ø 50 µm) with equal distance were transferred from microfabricated PDMS stamps using the micro-contact printing technique.[59] Patterns with center to center distances of 80 µm and 100 µm were used. PDMS stamps were incubated with 50 µg mL^{-1} Alexa Fluor 555-labeled BSA (A34786, Molecular Probes) at room temperature for 1 h, rinsed with DI water and blow-dried. The double-layer membranes were UV treated for 7 min for surface activation (Model 30, Jelight Company). The fluorescence markers were printed by pressing the PDMS stamp onto the membrane.

The strain and compression were calculated by quantifying the change of distance between two adjacent markers along and perpendicular to the stretching direction, respectively (Figure S2, Supporting Information). The strain/ compression fields were mapped based on the coordinates of the markers after stretching and the corresponding strain/compression using the MATLAB contour (Figures S3, S4, Supporting Information). The strain/compression fields were symmetrical based on the *x*-axis starting from the triangle's vertex for the triangular design in the stretch direction. For the square sample, the strain/compression field was symmetrical both in the *x* and *y* directions to the sample's center. To reduce variations during calibration, the strain/compression fields were averaged based on the respective symmetry axes for both designs.

Three samples for both designs were calibrated (Figures S3, S4, Supporting Information). To compare each sample's strain/compression fields, the strain/compression magnitude was plotted against the distance from the origin in the direction L1, L2, and L3 (Figures S3b,d, S4b,d, Supporting Information). For the triangular design, the origin was the vertex (Figures S3a, S4a, Supporting Information), and the L1 was the line starting from the vertex to the *x*-direction. L2 and L3 were acquired by rotating L1 for 15 and 30 degrees counterclockwise, respectively. For the square design, the origin was the square center (Figures S3c, S4c, Supporting Information), L1 started from the center to the *x*-direction, and L2 and

L3 were acquired by rotating L1 for 45 and 90 degrees counterclockwise, respectively. Data points close to the reference lines were used for quantifications (Figures S3a,c, S4a,c, Supporting Information). To compare the strain gradients, plots were linearly fitted to acquire slopes (Figures S3b,d, S4b,d, Supporting Information). Three slopes were obtained for reference lines L1 to L3 for each sample. One-way ANOVA test was used to compare individual samples using the slopes for both designs. No significant differences were found.

To quantify the stiffness of the PDMS membrane while applying the strain gradient, the stress–strain curve was obtained using a soft material-specific tensile machine (Mark-10 Force Gauge Model M7-5) (Figure S5, Supporting Information). The stiffness of the PDMS membrane remained constant between 0% to 30% of strain.

Fibronectin Distribution Analysis: HiLyte 488 -FN (FNR02, Cytoskeleton, INC) was coated on the double-layer membrane to directly visualize the FN distribution after applying strain gradient. 100 µL of 50 µg mL^{-1} HiLyte 488-FN was pipetted on the cell seeding area and incubated at 4 °C for 24 h while the membrane was stretched. Then the stretch was released to seed REFs at low density. After cells were attached overnight in a CO_2 incubator, the double-layer membrane was re-stretched, then the cells were incubated in Hoechst-medium mixture (R37605, ThermoFisher) for 30 min for nuclear staining, and then fixed in Fluoromount-G (0100-01 SouthernBiotech) at the stretched status on a glass slide for imaging.

To quantify the HiLyte 488-FN fluorescent intensity profile across the membrane, five lines were drawn using the plot profile function of ImageJ for each sample to automatically plot the intensities from the tip to the end along the lines (Figure S6, Supporting Information). Intensities were normalized by dividing the lowest value for each sample, and average intensities were quantified every 200 µm in the distance to quantify the significance (Figure S6b, Supporting Information). No significant differences were found from tip to end, indicating the uniform distributions of FN density across the membrane after stretching.

Visualization and Analysis of the Wrinkles Produced by Stretching: A confocal microscope (Leica ACCM) was used to directly visualize the linear wrinkles produced on the membrane after stretching a few times at the same magnitude (Figure S10a, Supporting Information). To quantify the distribution of the wrinkles, the intensity profile was quantified by drawing a straight line in the stretch direction from the tip to the end of the triangle using the plot profile function in ImageJ. The image's contrast was adjusted to enhance the wrinkle intensity. A peak of intensity was shown in the data for each wrinkle. Then peaks were identified using a customized MATLAB code. The distance between each adjacent peak and the frequency (number of wrinkles for 200 µm distance) were automatically calculated (Figure S10b,c, Supporting Information).

Microscopy for Cell Migration Trajectory: An epifluorescence microscope (Leica, DMi8) was used to image the cell migration trajectories and fluorescent signal calibrations. During the experiment, the device was kept in the 37 °C incubators for cell culture. The device was placed onto the microscope stage outside the incubator for imaging, which would take less than 2 min each time for each sample in the cell migration tracking experiment using the 10× phase contrast. Small air bubbles might be trapped underneath the corner of the cell culture area, which could be removed by lightly knocking the device one or two times. For the consistency of the culture condition, all samples would be subjected to the same knocking motion before imaging. The images were acquired every 50 min for the static strain condition, every 30 min for the cyclic strain condition for 6 h, and every 30 min for Bleb-treated static condition for 3 h.

The obtained image sequences were aligned by tracking two reference points that stayed at the constant location on the substrate for the entire experiment period. The reference points could be small particles left on the sample surface. The first image acquired after the stretching step was set to be the fixed image. The MATLAB fitgeotrans function was used for the translation and the imrotate function for the rotation to align the image sequence, allowing clear cell migration trajectories for tracking. Before cell tracking, lines on the image sequences were drawn to encircle the region of interest (Figure 2a). All cells with clear migration trajectories within the encircled region were tracked with the ImageJ MTrackJ plugin, and the direction angles were quantified using customized MATLAB codes. The representative cell tracking movies for six experiment groups were shown in Videos S1–S6, Supporting Information.

Device Modification for Focal Adhesion Imaging: The designs of the device were adjusted to allow high-resolution imaging for focal adhesion analysis. To minimize the distance between the cells and the objective, a glass bottom PDMS dish was specifically designed (Figure S15b, Supporting Information). 30 g of PDMS was poured into a 60 mm Petri dish to form a dish-shaped PDMS slab. A 20 × 46 mm cuboid was cut off in the middle, and then the opening was covered by plasma-bond a thin 24 × 50 mm cover slide. The dish was baked in a 65 °C oven overnight for firm bonding. The removable bottom of the device was redesigned as well (Figure S1, Supporting Information). A 60 mm diameter opening was laser cut on the removable acrylic bottom. The opening was designed to hold the PDMS dish properly, and small gaps were left for manual adjustment of the height of the PDMS dish during focal adhesion imaging.

To mitigate the interference of the PDMS membrane in the light path, the double-layer membrane was flipped to make cells face down during imaging (Figure S15, Supporting Information). To fit the cell culture sample into the PDMS dish, the glass slide was cut into smaller 20 × 14 mm pieces (Figure S15b, Supporting Information). The PDMS membrane and the silicone film base were bonded in the first step. The sample was then flipped to bond the glass slides on the opposite side of the PDMS membrane (Figure S15a, Supporting Information). As a result, when the adjusted double-layer membrane was mounted onto the device, the length of the silicone film was the same as the regular triangular sample, making the cells exposed to the same strain gradient and stretch magnitude as the cell tracking experiments. The sample was baked at 65 °C in an oven overnight for firm bonding after both steps, and then mounted onto the device. During the experiment, the device was flipped to coat FN and seeded cells on the bottom side of the PDMS membrane. Then the device was put into the incubator upside down for cells to attach for 1 h. The device was then flipped back and added 3–5 mL culture media into the PDMS dish. The culture media component was adjusted by replacing the DMEM with the non-phenol red type (21063029, Gibco). Other reagents remained the same.

Right after taking the first image, the cells were stretched once, and then the device was placed back into the incubator for 10 min before taking the second image. The time gap between two focal adhesion images was within 20 min. A 40× objective and YFP cube were used to image the focal adhesions.

Focal Adhesion and Protrusion/Retraction Image Processing and Quantification: The focal adhesion raw images were processed through ImageJ. Briefly, the background was removed with the Subtracted Background function using the Sliding paraboloid option. To enhance contrast, the CLAHE plugin was used with the Blocksize set to 19, Histogram bins set to 256, and the Maximum slope set to 6.[60] The Brightness/Contrast was further adjusted automatically to increase brightness. The focal adhesions were enhanced at this point. The image format was turned into 8 bits and adjusted the threshold automatically. The sizes and the coordinates of focal adhesions were quantified with the Analysis particle function.

The fluorescence intensity declined after cell stretching. Therefore, to effectively compare the focal adhesion dynamics within each cell, the data was normalized using images prior to stretching. The normalization was calculated as below:

$$P_{\mathrm{H}}^{\mathrm{N}} = \frac{A_{\mathrm{H2}} \times \frac{A_1}{A_2} - A_{\mathrm{H1}}}{A_{\mathrm{H1}}} \tag{1}$$

where A_1, A_{H1} are the focal adhesion size for the entire and one half of the cell before stretching, respectively; A_2, A_{H2} are the focal adhesion size for the entire and one half of the cell after stretching, respectively; and ${P_H}^N$ is the normalized percentage change of focal adhesion sizes in the respective half of the cell.

To quantify protrusion and retraction, the cell and the nuclei boundaries were manually encircled with dots using the ImageJ MTrackJ plugin. (Figure 4a,c). The dots were connected automatically with MATLAB to generate the boundaries. For each cell, the images before and after stretching were aligned with the mass center of the nucleus and the maximum gradient direction axis. The cell spreading areas were automatically quantified using the Analysis particle function.

Implementation of the Extended Motor-Clutch Model: An EMM was developed to simulate the interactions of cells and the elastic substrate based on the previously established model.[52,53] Briefly, the cell was simplified as a polygon, with the vertexes connecting to the elastic substrate with integrin-FN bonds. The randomly engaged bonds transmitted cell traction forces between cells and substrates. The on-rate and off-rate of the bonds control stochastic cell-substrate interactions. It was assumed that the vertex exposed to lower strain would be larger since it would naturally bind the substrate more easily. As such, the on-rate k_{on} would be larger at the lower strain side. Based on a previous study,[61] it was proposed that the on-rate and off-rate of integrin-FN bonds could be calculated as

$$k_{\mathrm{on}} = \frac{k_{\mathrm{on}}^{0}}{1 + e^{(\varepsilon - 0.16)/0.008}} \tag{2}$$

$$k_{\mathrm{off}} = 1.5\left(4.376e^{\left(0.1003F_{\mathrm{clutch}}/F_0\right)} + 0.004299e^{\left(-0.09225F_{\mathrm{clutch}}/F_0\right)}\right) \tag{3}$$

in which k_{on}^{0} and ϵ represent the reference on-rate and the local strain of substrates, respectively. $F_{\mathrm{clutch}} = k_{\mathrm{c}}\ (x_{\mathrm{c}} - x_{\mathrm{sub}})$ is the clutch force of a single integrin—FN bond. k_{c} is the spring constant, x_{c} is the displacement of bond on the filament, and x_{sub} is the substrate displacement. $F_0 = 1$ pN is the reference force magnitude to normalize F_{clutch}. With the engagement of integrin-fibronectin pairs, the substrate displacement can be calculated from

$$x_{\mathrm{sub}} = \frac{k_{\mathrm{c}}\sum_{i=1}^{n_{\mathrm{eng}}} x_{\mathrm{c},i}}{k_{\mathrm{s}} + n_{\mathrm{eng}}k_{\mathrm{c}}} \tag{4}$$

where n_{eng} is the number of the engaged bonds on the filament and $x_{\mathrm{c},\,i}$ is the displacement of the i^{th} bond on the filament. According to Cerruti problem, spring constant of substrate k_{s} can be calculated by:[52]

$$k_{\mathrm{s}} = 2\pi Ga/\ (2 - \nu) \tag{5}$$

where ν is the Poisson ratio and $G = E/2(1 + \nu)$.

The cell migration can be modeled by the motion equation of each vertex, which is given by:

$$\mu dr_{\mathrm{i}}/dt = -\nabla_{\mathrm{i}}\left(U_{\mathrm{shape}}\right) + \mu\left(V_{\mathrm{P}} + V_{\mathrm{r}}\right) n_{\mathrm{i}}^{p} \tag{6}$$

where μ is the friction coefficient. The first term is constituted by contraction force f_i^{l}, area constraint force f_i^{a} and bending force f_i^{b} (Figure 5a).[52] The second term is the cell polarization force, where V_{P} and V_{r} are the polymerization and retrogradation flow speed along the orientation of each filament n_i^{p}, respectively. Retrogradation flow velocity is determined by cell tractions,[53] and can be calculated as

$$V_{\mathrm{r}} = V_0\left(1 - F^{\mathrm{trac}}/N_{\mathrm{m}}F_{\mathrm{m}}\right) \tag{7}$$

where V_0 is the unloading velocity of each filament and $F^{\mathrm{trac}} = k_{\mathrm{s}}\,x_{\mathrm{sub}}$ is the total traction force magnitude exerted by the filament. N_{m} is the number of myosin motors, whose stall force is denoted by F_{m}. The myosin motors exert cell contractions along filaments. These simulations were implemented on MATLAB, and detailed parameters are provided in Table **S1**, Supporting Information.

Statistics: Statistical analysis was performed using OriginLab and R. Rayleigh tests were used to determine the unimodal distribution of circular data in cell migration direction analysis.[62] For non-circular datasets, normality tests were run to determine the normality of the distribution. For statistical comparisons of two normal distributed datasets, *p*-values were calculated using the two-sample *t*-test. For statistical comparisons of two non-normal distributed datasets, *p*-values were calculated using the non-parametric Mann–Whitney test. For statistical comparisons of multiple normal distributed datasets, *p*-values were calculated using the one-way ANOVA test.

Supporting Information

Supporting Information is available from the Wiley Online Library or from the author.

Acknowledgements

This work was supported by the National Science Foundation (CMMI 1846866 to Y.S.), the National Institute of Diabetes and Digestive and Kidney Diseases (R01DK129990 to Y.S.), National Natural Science Foundation of China (Grant No. 12272202 to B.L.), and in part by grants from the Human Frontier Science Program (RGP0038/2018) (to D.-H.K.), the Ministry of Trade, Industry and Energy (MOTIE) and Korea Institute for Advancement of Technology (KIAT) through the International Cooperative R&D program (Project No. P0004638 to D.-H.K.).

Conflict of Interest

The authors declare no conflict of interest.

Author Contributions

F.Y. designed and performed the experiments, analyzed the data, and wrote the manuscript. P.C. performed the simulation and wrote the manuscript. T.X. microfabricated micropatterned stamps. H.J. performed tensile testing. Y.Su., B.L., Y.Sh., and D.K. supervised the project. All authors edited and approved the manuscript.

Data Availability Statement

The data that support the findings of this study are available from the corresponding author upon reasonable request.

Keywords

cell stretching devices, focal adhesion, mechanotransduction, motor-clutch model, single cell migration, strain gradient, tensotaxis, traction force

Received: June 20, 2023
Revised: August 27, 2023

---

[1] N. M. E. Ayad, S. Kaushik, V. M. Weaver, *Philos. Trans. R. Soc., B* **2019**, *374*, 20180215.
[2] M. A. Swartz, M. E. Fleury, *Annu. Rev. Biomed. Eng.* **2007**, *9*, 229.
[3] Y. Sun, C. S. Chen, J. Fu, *Annu. Rev. Biophys.* **2012**, *41*, 519.
[4] O. J. Abilez, E. Tzatzalos, H. Yang, M.-T. Zhao, G. Jung, A. M. Zöllner, M. Tiburcy, J. Riegler, E. Matsa, P. Shukla, Y. Zhuge, T. Chour, V. C. Chen, P. W. Burridge, I. Karakikes, E. Kuhl, D. Bernstein, L. A. Couture, J. D. Gold, W. H. Zimmermann, J. C. Wu, *Stem Cells* **2017**, *36*, 265.
[5] S. A. Gudipaty, J. Lindblom, P. D. Loftus, M. J. Redd, K. Edes, C. F. Davey, V. Krishnegowda, J. Rosenblatt, *Nature* **2017**, *543*, 118.

[6] F. Serwane, A. Mongera, P. Rowghanian, D. A. Kealhofer, A. A. Lucio, Z. M. Hockenbery, O. Campàs, *Nat. Methods* **2017**, *14*, 181.
[7] M. Von Dassow, L. A. Davidson, *Dev. Dyn.* **2009**, *238*, 2.
[8] L. V. Beloussov, N. N. Louchinskaia, A. A. Stein, *Dev. Genes Evol.* **2000**, *210*, 92.
[9] H. Wang, W. Ip, R. Boissy, E. S. Grood, *J. Biomech.* **1995**, *28*, 1543.
[10] H. Abiko, S. Fujiwara, K. Ohashi, R. Hiatari, T. Mashiko, N. Sakamoto, M. Sato, K. Mizuno, *J. Cell Sci.* **2015**, *128*, 1683.
[11] A. Livne, E. Bouchbinder, B. Geiger, *Nat. Commun.* **2014**, *5*, 3938.
[12] G. Reig, M. Cerda, N. Sepúlveda, D. Flores, V. Castañeda, M. Tada, S. Härtel, M. L. Concha, *Nat. Commun.* **2017**, *8*, 15431.
[13] S. Márquez, G. Reig, M. Concha, R. Soto, *Phys Biol* **2019**, *16*, 066001.
[14] P. J. M. van Haastert, P. N. Devreotes, *Nat. Rev. Mol. Cell Biol.* **2004**, *5*, 626.
[15] S. B. Carter, *Nature* **1967**, *213*, 256.
[16] S. G. Ricoult, T. E. Kennedy, D. Juncker, *Front. Bioeng. Biotechnol.* **2015**, *3*, 40.
[17] J. Park, D.-H. Kim, A. Levchenko, *Biophys. J.* **2018**, *114*, 1257.
[18] C.-M. Lo, H.-B. Wang, M. Dembo, Y.-L. Wang, *Biophys. J.* **2000**, *79*, 144.
[19] A. Isomursu, K. Y. Park, J. Hou, B. Cheng, M. Mathieu, G. A. Shamsan, B. Fuller, J. Kasim, M. M. Mahmoodi, T. Lu, G. M. Genin, F. Xu, M. Lin, M. D. Distefano, J. Ivaska, D. J. Odde, *Nat. Mater.* **2022**, *21*, 1081.
[20] W. J. Richardson, R. P. Metz, M. R. Moreno, E. Wilson, J. E. Moore Jr., *J. Biomech. Eng.* **2011**, *133*, 101008.
[21] S.-L. i. Lin, J.-C. Yang, K.-N. Ho, C.-H. Wang, C.-W. u. Yeh, H.-M. Huang, *Med. Biol. Eng. Comput.* **2009**, *47*, 1273.
[22] J. Bueno, Y. Bazilevs, R. Juanes, H. Gomez, H. Gomez, *Extreme Mech. Lett.* **2017**, *13*, 10.
[23] G. S. Rosalem, E. B. Las Casas, T. P. Lima, L. A. González-Torres, *Biomech. Model. Mechanobiol.* **2020**, *19*, 1537.
[24] Y. u. C. Yung, H. Vandenburgh, D. J. Mooney, *J. Biomech.* **2009**, *42*, 178.
[25] S. Chagnon-Lessard, H. Jean-Ruel, M. Godin, A. E. Pelling, *Integr. Biol.* **2017**, *9*, 607.
[26] Y. Morita, T. Sato, S. Watanabe, Y. Ju, *Exp. Mech.* **2015**, *55*, 635.
[27] L. Wang, Y. Li, B. Chen, S. Liu, M. Li, L. Zheng, P. Wang, T. Lu, F. Xu, *ACS Appl. Mater. Interfaces* **2015**, *7*, 1508815097.
[28] J. Lu, X. Zou, Z. Zhao, Z. Mu, Y. Zhao, Z. Gu, *ACS Appl. Mater. Interfaces* **2015**, *7*, 10091.
[29] I. D. Johnston, D. K. Mccluskey, C. K. L. Tan, M. C. Tracey, *J. Micromech. Microeng.* **2014**, *24*, 035017.
[30] M. Liu, J. Sun, Y. Sun, C. Bock, Q. Chen, *J. Micromech. Microeng.* **2009**, *19*, 035028.
[31] H. M. Langevin, K. N. Storch, M. J. Cipolla, S. L. White, T. R. Buttolph, D. J. Taatjes, *Histochem. Cell Biol.* **2006**, *125*, 487.
[32] D. Tremblay, S. Chagnon-Lessard, M. Mirzaei, A. E. Pelling, M. Godin, *Biotechnol. Lett.* **2014**, *36*, 657.
[33] D. Huh, B. D. Matthews, A. Mammoto, M. Montoya-Zavala, H. Y. Hsin, D. E. Ingber, *Science* **2010**, *328*, 1662.
[34] S. Halldorsson, E. Lucumi, R. Gómez-Sjöberg, R. M. T. Fleming, *Biosens. Bioelectron.* **2015**, *63*, 218.
[35] J. B. Freund, J. G. Goetz, K. L. Hill, J. Vermot, *Development* **2012**, *139*, 1229.
[36] M. Versaevel, L. Alaimo, V. Seveau, M. Luciano, D. Mohammed, C. Bruyère, E. Vercruysse, O. Théodoly, S. Gabriele, *Sci. Rep.* **2021**, *11*.
[37] Z. Roveimiab, F. Lin, J. E. Anderson, *Am. J. Physiol.: Cell Physiol.* **2020**, *319*, C75.
[38] A. Katsumi, J. Milanini, W. B. Kiosses, M. A. Del Pozo, R. Kaunas, S. Chien, K. M. Hahn, M. A. Schwartz, *Cell Biol.* **2002**, *158*, 153.
[39] S. Munevar, Y.-L. Wang, M. Dembo, *Stem Cells Int.* **2004**, *117*, 85.
[40] B. Geiger, K. M. Yamada, *Cold Spring Harbor Perspect. Biol.* **2011**, *3*, a005033.
[41] E. F. Foxman, E. J. Kunkel, E. C. Butcher, *J. Cell Biol.* **1999**, *147*, 577.
[42] G. Malet-Engra, W. Yu, A. Oldani, J. Rey-Barroso, N. S. Gov, G. Scita, L. Dupré, *Curr. Biol.* **2015**, *25*, 242.
[43] B. J. Duchez, A. D. Doyle, E. K. Dimitriadis, K. M. Yamada, *Biophys. J.* **2019**, *116*, 670.
[44] X. Trepat, Z. Chen, K. Jacobson, *Compr. Physiol.* **2012**, *2*, 2369.
[45] S. Weng, Y. Shao, W. Chen, J. Fu, *Nat. Mater.* **2016**, *15*, 961.
[46] C. Okimura, K. Ueda, Y. Sakumura, Y. Iwadate, *Cell Adhes. Migr.* **2016**, *10*, 331.
[47] A. M. Pasapera, I. C. Schneider, E. Rericha, D. D. Schlaepfer, C. M. Waterman, *J. Cell Biol.* **2010**, *188*, 877.
[48] M. Vicente-Manzanares, *Curr. Biol.* **2013**, *23*, R28.
[49] H. H. Wang, H. Tanaka, X. Qin, T. Zhao, L. i.-H. Ye, T. Okagaki, T. Katayama, A. Nakamura, R. Ishikawa, S. E. Thatcher, G. L. Wright, K. Kohama, *Am. J. Physiol.: Heart Circ. Physiol.* **2008**, *294*, H2060.
[50] W. Y. Wang, C. D. Davidson, D. Lin, B. M. Baker, *Nat. Commun.* **2019**, *10*, 1186.
[51] Z. Liu, L. A. Van Grunsven, E. Van Rossen, B. Schroyen, J.-P. Timmermans, A. Geerts, H. Reynaert, *Br. J. Pharmacol.* **2009**, *159*, 304.
[52] P.-C. Chen, X. i.-Q. Feng, B. o. Li, *Biophys. J.* **2022**, *121*, 3474.
[53] C. E. Chan, D. J. Odde, *Science* **2008**, *322*, 1687.
[54] S. V. Plotnikov, A. M. Pasapera, B. Sabass, C. M. Waterman, *Cell* **2012**, *151*, 1513.
[55] D. B. Wormer, K. A. Davis, J. H. Henderson, C. E. Turner, *PLoS One* **2014**, *9*, e91815.
[56] S. Wong, W. Guo, Y. Wang, *Proc. Natl. Acad. Sci. U. S. A.* **2014**, *111*, 17176.
[57] M. Raab, J. Swift, P. C. D. P. Dingal, P. Shah, J.-W. Shin, D. E. Discher, *J. Cell Biol.* **2012**, *199*, 669.
[58] T. H. N. Dinh, E. Martincic, E. Dufour-Gergam, P. Y. Joubert, *J. Sens.* **2017**, *2017*, 8235729.
[59] D. Qin, Y. Xia, G. M. Whitesides, *Nat. Protoc.* **2010**, *5*, 491.
[60] U. Horzum, B. Ozdil, D. Pesen-Okvur, *MethodsX* **2014**, *1*, 56.
[61] A. Elosegui-Artola, E. Bazellières, M. D. Allen, I. Andreu, R. Oria, R. Sunyer, J. J. Gomm, J. F. Marshall, J. L. Jones, X. Trepat, P. Roca-Cusachs, *Nat. Mater.* **2014**, *13*, 631.
[62] L. Landler, G. D. Ruxton, E. P. Malkemper, *Behav. Ecol. Sociobiol.* **2018**, *72*, 128.